Nanomanufacturing and Metrology (2023) 6:17
https://doi.org/10.1007/s41871-023-00195-5

ORIGINAL ARTICLE

Semi-analytical Stiffness Model of Bolted Joints in Machine Tools Considering the Coupling Effect

Yiwei Ma[1] · Yutao Fu[2] · Yanling Tian[1] · Xianping Liu[1]

Received: 24 December 2022 / Revised: 20 March 2023 / Accepted: 27 March 2023

Abstract

This study proposes an improved semi-analytical approach for contact stiffness modeling of bolted joints in a machine tool system. First, nonlinear contact stress distribution within a single-bolted joint is obtained from the simulation results of finite element analysis software. Second, employing the Hertz contact theory and fractal theory, the contact stiffness model of a single asperity is formulated, affording analytical expressions for normal and tangential contact stiffnesses of a single-bolted joint by integrating multi-asperities in the contact area. Subsequently, considering two test specimens as illustrations, the mode shapes and natural frequencies of the proposed model and modal analysis tests are compared, and the influence of coupling effects between two adjacent bolts is illustrated. The maximum error in the natural frequencies of the proposed approach is < 2.73% relative to the experimental results. Finally, the measurements of frequency response functions on a box-in-box precision horizontal machine tool are conducted to demonstrate the accuracy and efficiency of the proposed model. The proposed model is highly efficient in revealing the influence of microcontact factors on the contact stiffness of bolted joints and in guiding the optimal functional design of bolt arrangements under the framework of virtual machine tools.

Highlights

1. A nonlinear contact stress distribution in a single-bolted joint is proposed using a negative exponential function.
2. A single-bolted joint's normal and tangential contact stiffnesses are derived considering the coupling effect.
3. A modal experiment is conducted on two designed test specimens to demonstrate the accuracy of the proposed model.

Keywords Stiffness modeling · Bolted joint · Microcontact mechanics · Fractal theory · Rough surface

List of Symbols

$z(x)$	Height of the surface topography
D, G	Fractal dimensions and roughness
γ	Spectrum of the surface topography
x	Coordinate of the measurement point
l	Sample length topography
a	Microcontact area
a_c	Critical microcontact area
a_l	Largest microcontact area
A	Real contact area
A_e	Elastic contact area
A_p	Plastic contact area
r	Radius of the microcontact area
R	Radius of a single asperity
δ	Deformation height of a single asperity
δ_c	Critical deformation height determining the elastic or plastic deformation
α, β	Coefficients of a single-bolted joint's contact area

✉ Yiwei Ma
Yi-Wei.Ma@warwick.ac.uk

Yutao Fu
fuyutao2468@tju.edu.cn

Yanling Tian
Y.Tian.1@warwick.ac.uk

Xianping Liu
X.Liu@warwick.ac.uk

1 School of Engineering, The University of Warwick, Coventry CV4 7AL, UK

2 School of Mechanical Engineering, Tianjin University, Tianjin 300072, China

Published online: 15 May 2023

$p_n(r)$	Normal contact stress
r_0	Radius of a single bolt
R_0	Radius of the contact area of a single-bolted joint
η	Scaling factor
P	Equivalent normal resultant force of a single-bolted joint's contact area
$\overline{P}$	Equivalent tangential resultant force of a single-bolted joint's contact area
p	Normal load of a spherical asperity
$\overline{p}$	Tangential load of a spherical asperity
p_e	Elastic load of a spherical asperity
p_p	Plastic load of a spherical asperity
d_0	Center distance between two adjacent bolts
θ_0	Contact angle
σ_y	Yield strength of the contact surface
H	Hardness of the contact surface
E'	Equivalent elastic modulus
G'	Equivalent shear modulus
v_1, v_2	Poisson's ratio of two contact surfaces
E_1, E_2	Elastic modulus of the two contact surfaces
$n(a)$	Distribution density function of multi-asperities
ε	Shear deformation
μ	Coefficient of sliding friction
ψ	Domain extension parameter
k_n	Normal contact stiffness of a single asperity
K_n	Normal contact stiffness of a single-bolted joint
c_t	Tangential compliance of a single asperity
k_t	Tangential contact stiffness of a single asperity
K_t	Tangential contact stiffness of a single-bolted joint
$S(\tau)$	Function of the rough surface profile
$N-n$	Number of calculation data
τ	Arbitrary interval
$\boldsymbol{\Phi}_{\mathrm{FE},i}$, $\boldsymbol{\Phi}_{\mathrm{MT},j}$	ith and jth mode shapes of the FE model and the developed modal test

Abbreviations

PIM	Parameter identification method
FT	Fractal theory
EMM	Equivalent material method
FRF	Frequency response function
GW	Greenwood and Williamson
MB	Majumdar and Bhushan
WN	Weierstrass and Mandelbrot
FEA	Finite element analysis
MAC	Modal assurance criterion

1 Introduction

Because of its simplicity and stability in assembly and manufacturing, the bolted joint is an important mechanical connection used in the crucial equipment of multiple industrial areas, including aerospace, automobiles, energy, and shipping [1, 2]. The contact stiffness of the bolted joint is an important performance of machine tools, representing the safety and reliability of the fixed joint [3–5]. Considering the complexity and nonlinearity resulting from factors such as material properties, contact pressure, and surface roughness, a simplified contact stiffness model of the bolted joint is required at the initial conceptual design stage to accurately and efficiently predict the characteristics of the fixed joint in machine tools.

The available methods for contact stiffness modeling of bolted joints can be roughly categorized into three types, i.e., parameter identification method (PIM) [6–13], fractal theory (FT) [14–26], and equivalent material method (EMM) [27–34]. The contact elasticity of bolted joints in the PIM is treated as a system comprising several springs and damping, which are adjusted iteratively from the frequency response function (FRF) comparison studies of modal analysis tests and identified parameters. For instance, Mao et al. proposed a general dynamic model of fixed joints considering the coupling effects between substructures and used the model to identify the stiffness parameters of fixed joints according to the inverse relationship between the dynamic stiffness matrix and FRF matrix [6]. The maximum error in the proposed model relative to the experimental results was < 10%. Based on the established identification model, they illustrated that the contact stiffnesses of bolted joints under different material combinations were proportional to the equivalent elastic modulus, consistent with the Hertz contact theory [8]. The equivalent stiffness and Valanis parameters of a metric M12 bolted joint were determined from quasistatic experiments [9]. Li et al. proposed an improved nonlinear approach for the microslip modeling of bolted joints considering residual shear deformation and identified the parameters in the hysteresis loop through quasistatic experiments [13]. According to the experimental results, the identified stiffness parameters in the PIM are relatively accurate. However, this method is typically appropriate for model verification or database generation under different conditions owing to repeatedly time-consuming measurements.

To investigate the influence of various factors on the contact stiffness of rough surfaces, a simplified theoretical calculation model is required. During the development of microscopy technology, scholars discovered that metal surfaces exhibit statistical self-similarity and self-affinity at different scales. Thus, the FT was proposed [14, 15]. In FT, the characteristics of bolted joints are described from a single asperity and then extended to the entire joint surface according to the distribution of asperities, including the Greenwood and Williamson (GW) model, Persson's model, and Majumdar and Bhushan (MB) model. To calculate the normal contact stiffness accurately and effectively, Liu et al. proposed an improved fractal model by introducing a specific coefficient related to friction, which helped reveal the influence of friction on the dynamic performance of the contact area [16]. Considering the differences in deformation regimes, Xiao et al. formulated a novel expression for normal contact stiffness between rough surfaces [20]. The deformation modes of a single asperity were determined as fully elastic, elastoplastic, and fully plastic, which changed smoothly at critical points between different deformation regimes. Subsequently, Zhang et al. introduced a novel parameter associated with the contact angle between the upper and lower asperities of rough surfaces, establishing a normal contact stiffness model considering the oblique contact mode [24]. Experiments demonstrated that the modified model was more accurate and appropriate than the previous models in predicting the contact stiffness of surfaces with larger fractal dimensions. Considering the inclination angle, Liu et al. proposed normal and tangential contact stiffness models of the bolted joint surface of a heavy-duty machine tool [25]. Combining the contact mechanism at macro- and microscales, Chang et al. established a hybrid contact stiffness model for bolted joints [26]. By replacing M10 bolts with M8 bolts, a 2.283% reduction was achieved in the dynamic response of the workpiece in a machine tool by optimizing the bolt arrangement. Although the FT provides valuable information concerning the contact characteristics on a microscale, it neglects the stress distribution on a rough surface.

The joint surface in the EMM is treated as a virtual material layer whose material properties are obtained from the above theoretical calculation model. This approach is advantageous because it can be easily integrated into an FEA (finite element analysis) program. For instance, Tian et al. assumed the microcontact area of contact surfaces in the fixed joint as a virtual isotropic material and then derived analytical expressions for the elastic modulus, Poisson ratio, shear modulus, and density by considering normal and tangential characteristics [27]. The experimental results illustrated that the mode shapes of the specimen estimated by the theoretical model agreed very well with those obtained from the modal analysis tests, and the differences between the natural frequencies of the two models were less than 9%. Liao et al. employed an orthogonal virtual material model to

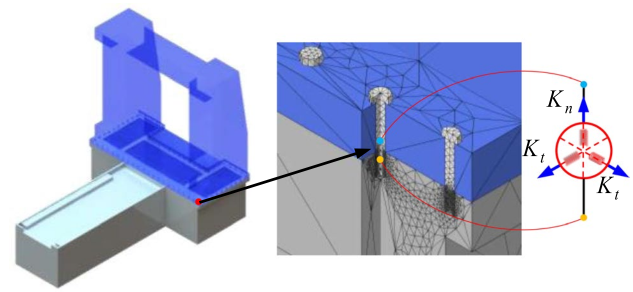

Fig. 1 Schematic of the equivalent elastic model of a single-bolted joint

describe the properties of a joint contact surface, which was divided into several sublayers, thereby deducing a novel equivalent gradient material model [29]. Assuming an uneven stress distribution on a contact surface, Zhao et al. presented a nonlinear equivalent material model to accurately predict the performances of a bolted joint assembly [31]. Zhang et al. derived the expressions for the equivalent material properties based on the oblique asperity contact FT and demonstrated that a bolted joint with small size, large roughness, and tightening torque displayed a more pronounced effect of EM (equivalent material) [33]. A novel EM model was proposed by Yang et al. to predict the lower-order natural frequencies of composite bolted joints with carbon fiber-reinforced plastic, which was crucial in the optimization design of the composite material [34]. However, the coupling effects between the adjacent bolted joints were ignored in the existing FT and EMM, which is an important issue when determining a bolt arrangement.

To sufficiently guide the optimization design of bolt arrangements, this paper introduces a semi-analytical stiffness model for bolted joints in a machine tool system. This work provides accurate and efficient modeling of bolted joints considering the nonlinear stress distribution and coupling effects between adjacent bolts. Following a brief introduction to stiffness modeling methodologies, an enhanced contact stiffness model for bolted joints combining FT and FEA is presented. This model simulates the nonlinear pressure distribution inside the contact area of a bolted joint using FEA, affording fractal-based analytical expressions for normal and tangential contact stiffnesses. Then, two groups of test specimens are considered as an illustration and comparison studies between the proposed model and modal analysis tests are conducted to demonstrate the accuracy and validity of the proposed model. Further, a box-in-box precision horizontal machine tool is used to verify the developed contact stiffness model. Finally, several conclusions of this paper are summarized.

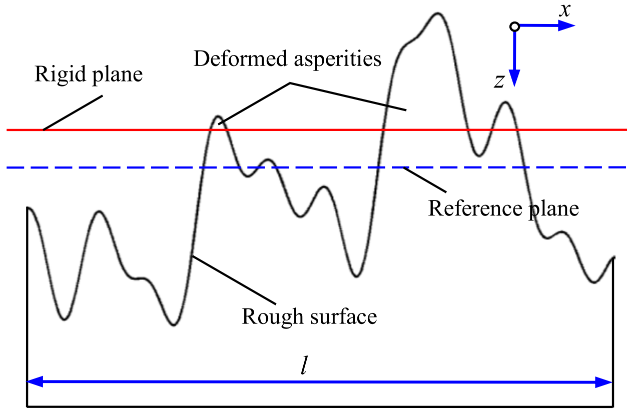

Fig. 2 Contact model of a rigid plane with a rough surface

2 Contact Stiffness Modeling of a Bolted Joint

In this section, we develop semi-analytical expressions for the normal and tangential contact stiffnesses of a single-bolted joint considering nonlinear contact stress distribution and coupling effects. Figure 1 shows the schematic diagram of a single-bolted joint in a machine tool system, and the equivalent elastic model of a single-bolted joint is considered to be a three-dimensional spring.

2.1 Fractal Model of Rough Surfaces

In this subsection, we introduce the fractal model of the rough surface. The micromodel of two contact surfaces can be simplified as the contact of a rigid plane with a rough surface, whose two-dimensional topography is illustrated in Fig. 2. Based on the Weierstrass and Mandelbrot (WM) fractal function, the height of surface topography can be described by the superposition of several cosine waves as [35]

$$z(x) = G^{D-1} \sum_{n=0}^{\infty} \frac{\cos 2\pi\gamma^n x}{\gamma^{(2-D)n}} \tag{1}$$

where $D \in (1, 2)$ and G denote the fractal dimension and roughness parameters of the surface topology, which represent the irregularity and amplitude of $z(x)$ at the sample length, respectively. x represents the coordinate of the measurement point, and $\gamma > 1$ is the spectrum of the surface topography. For most rough surfaces, $\gamma = 1.5$. n denotes the number of cosine waves.

Based on the assumptions of the WM model, the deformed asperities between two rough surfaces are treated as hemispheres. The contact model is shown in Fig. 3. Considering the sample length on the rough surface, the topography can be described as

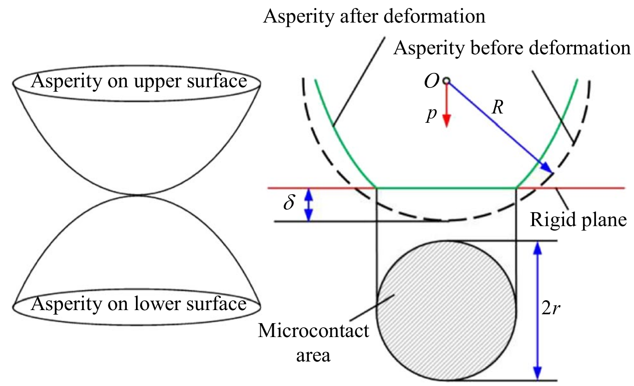

Fig. 3 Normal contact of a single asperity condensed by a rigid plane

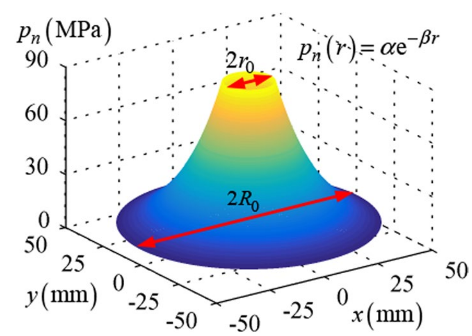

Fig. 4 Distribution of normal contact stress in a single-bolted joint

$$z(x) = G^{D-1} l^{2-D} \cos \frac{\pi x}{l}, \quad x \in \left(-\frac{l}{2}, \frac{l}{2}\right) \tag{2}$$

where $l = a^{0.5}$ denotes the sample length topography, and $a = \pi r^2$ is the microcontact area. r represents the radius of the microcontact area. Therefore, radius R and interference δ of a single asperity are derived as

$$R = \left| 1 \Big/ \left| \frac{d^2 z(x)}{dx^2} \right|_{x=0} \right| = \frac{a^{0.5D}}{\pi^2 G^{D-1}}, \quad \delta = G^{D-1} l^{2-D} = G^{D-1} a^{1-0.5D} \tag{3}$$

where δ represents the deformation height of the top of a single asperity, as shown in Fig. 3.

2.2 Simulation of the Contact Stress Distribution

According to the FEA simulation, normal contact pressure undergoes exponential decay along the radial axis within the contact area of a single-bolted joint, as shown in Fig. 4. The normal contact stress in the contact area is described by a negative exponential function as

$$p_n(r) = \alpha e^{-\beta r} \text{ (MPa)} \tag{4}$$

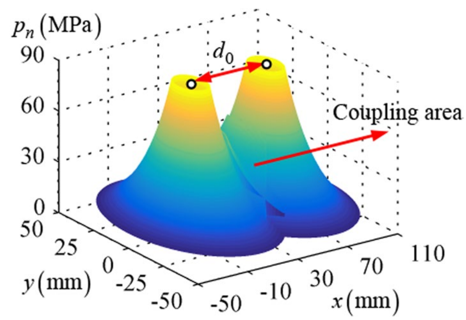

Fig. 5 Distributions of normal contact stress in two adjacent bolted joints

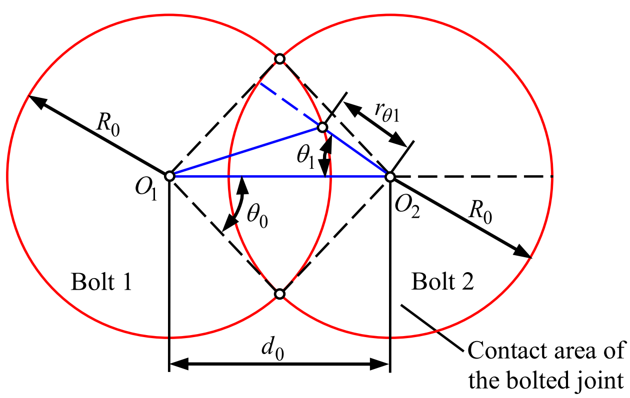

Fig. 6 Geometrical parameters of two adjacent bolted joints

where α and β are coefficients, which are both related to the geometry, preload, and material properties of a single-bolted joint's contact area and can be calculated from FE (finite element) software. The contact area of a single-bolted joint is then described as a hollow ring with a radius $r \in \left(r_0, R_0\right)$, where R_0 is defined by

$$p_{\mathrm{n}}\left(R_0\right) = \eta p_{\mathrm{n,max}} \tag{5}$$

where $\eta \in (0, 1)$ is the scaling factor. Subsequently, we consider the distributions of the normal contact stress of two adjacent bolted joints, as shown in Fig. 5. Each single-bolted joint has the same distribution of contact stress, as shown in Fig. 4. The overlapping area of two contact areas is the coupling area of two adjacent bolted joints, where the normal contact stress is cumulative in this area, as shown in Fig. 6. Therefore, the equivalent normal resultant force in the contact area of a single-bolted joint is described as

$$\begin{aligned} P = & \int_{-\pi}^{\pi} \int_{0}^{R_0} p_{\mathrm{n}}(r) \mathrm{d}r \mathrm{d}\theta + \int_{-\pi}^{-\pi+\theta_0} \int_{r_{\theta 1}}^{R_0} p_{\mathrm{n}}(r) \mathrm{d}r \mathrm{d}\theta \\ & + \int_{\pi-\theta_0}^{\pi} \int_{r_{\theta 1}}^{R_0} p_{\mathrm{n}}(r) \mathrm{d}r \mathrm{d}\theta \end{aligned} \tag{6}$$

where θ_0 is the contact angle related to the center distance d_0 between two adjacent bolts and R_0, as shown in Fig. 6. $r_{\theta 1}$ is a function of θ_1 and is solved by

$$r_{\theta 1} = d_0 \cos\theta_1 - \sqrt{R_0^2 - d_0^2\left(1 - \cos^2\theta_1\right)} \tag{7}$$

2.3 Model of a Single Asperity and Multi-asperities

The critical deformation height determining the elastic or plastic deformation of the spherical asperities is

$$\begin{aligned} & \delta_{\mathrm{c}} = \left(\frac{\pi k \phi}{2}\right)^2 R = \left(\frac{k\phi}{2}\right)^2 \frac{a^{0.5D}}{G^{D-1}} \\ & k = H/\sigma_{\mathrm{y}}, \quad \phi = \sigma_{\mathrm{y}}/E', \quad E' = \left(\frac{1-v_1^2}{E_1} + \frac{1-v_2^2}{E_2}\right)^{-1} \end{aligned} \tag{8}$$

where σ_{y} and H denote the yield strength and hardness of the softer material between the lower and upper rough surfaces, respectively. E' represents the equivalent elastic modulus. $v_1(E_1)$ and $v_2(E_2)$ represent the Poisson's ratio (elastic modulus) of two contact surfaces. If $\delta > \delta_{\mathrm{c}}$, then the asperity is in plastic deformation; otherwise, it is in elastic deformation. Obviously, δ_{c} is a constant value, and it only corresponds to the material properties. Substituting Eq. (3) into Eq. (8) leads to

$$a_{\mathrm{c}} = G^2 \left(\frac{k\phi}{2}\right)^{\frac{2}{1-D}} \tag{9}$$

where a_{c} represents the critical contact area of the asperities, which is associated only with fractal parameters and material properties. If $a > a_{\mathrm{c}}$, then the asperity is in elastic deformation; otherwise, it is in plastic deformation.

Based on the Hertz contact theory, the plastic or elastic loads on a spherical asperity are described as

$$p = \begin{cases} p_{\mathrm{e}} = \frac{4}{3} E' R^{0.5} \delta^{1.5} = \frac{4}{3\pi} E' G^{D-1} a^{1.5-0.5D}, & a > a_{\mathrm{c}} \\ p_{\mathrm{p}} = k \sigma_{\mathrm{y}} a, & a < a_{\mathrm{c}} \end{cases} \tag{10}$$

The multi-asperities during the contact area satisfy the following distribution density function [36]

$$n(a) = 0.5D\psi^{1-0.5D} a_1^{0.5D} a^{-1-0.5D}, \quad 0 \le a \le a_1 \tag{11}$$

where $\psi > 1$ denotes the domain extension parameter of the microcontact area, and a_1 represents the largest microcontact area. ψ is obtained as

$$\psi^{1-0.5D} - \left(1 + \psi^{-0.5D}\right)^{0.5D-1} = 2/D - 1 \tag{12}$$

Then, the real contact area A, the elastic contact area A_e, and the plastic contact area A_p are derived as

$$\begin{aligned} A &= \int_0^{a_1} n(a)a\mathrm{d}a = \frac{D\psi^{1-0.5D}}{2-D}a_1 \\ A_e &= \int_{a_c}^{a_1} n(a)a\mathrm{d}a = \frac{D\psi^{1-0.5D}}{2-D}\left(a_1 - a_1^{D/2}a_c^{(2-D)/2}\right) \\ A_p &= \int_0^{a_c} n(a)a\mathrm{d}a = \frac{D\psi^{1-0.5D}}{2-D}a_1^{D/2}a_c^{(2-D)/2} \end{aligned} \tag{13}$$

Integrating the plastic and elastic loadings inside the contact area obtains the resultant normal force:

$$\begin{aligned} P &= P_e + P_p \\ &= \frac{4}{3\pi}E'G^{D-1}\int_{a_c}^{a_1} n(a)a^{1.5-0.5D}\mathrm{d}a + k\sigma_y\int_0^{a_c} n(a)a\mathrm{d}a \end{aligned} \tag{14}$$

Substituting Eq. (11) into Eq. (14) leads to

$$P = \begin{cases} \psi^{0.25}\left(\frac{E'\sqrt{G}a_1^{0.75}}{\pi}\ln\frac{a_1}{a_c} + 1.5k\sigma_y a_1^{0.75}a_c^{0.25}\right) & D = 1.5 \\ \psi^{1-0.5D}D\left(\begin{array}{l}\frac{4E'G^{D-1}a_1^{0.5D}}{3\pi(3-2D)}\left(a_1^{1.5-D} - a_c^{1.5-D}\right) \\ +\frac{k\sigma_y a_c^{1-0.5D}a_1^{0.5D}}{2(2-D)}\end{array}\right) & D \neq 1.5 \end{cases} \tag{15}$$

Equation (15) clearly shows that P is associated with a_1, which can be resolved by combing Eqs. (6) and (15).

2.4 Normal and Tangential Stiffness Model of a Bolted Joint

Following the Hertz contact theory, the interference δ and the radius of the contact area of a single asperity can be described as

$$\delta = \frac{r^2}{R} = \left(\frac{9}{16}\frac{p^2}{RE'^2}\right)^{\frac{1}{3}}, \quad r = \left(\frac{3pR}{4E'}\right)^{\frac{1}{3}} \tag{16}$$

The normal contact stiffness of a single asperity is then derived as

$$k_n = \frac{\mathrm{d}p}{\mathrm{d}\delta} = 2E'\sqrt{R\delta} = 2E'r = 2E'\sqrt{\frac{a}{\pi}} \tag{17}$$

Integrating k_n within the contact area leads to the normal contact stiffness of a single-bolted joint

$$K_n = \int_{a_c}^{a_1} k_n n(a)\mathrm{d}a \tag{18}$$

Substituting Eqs. (11) and Eq. (17) into Eq. (18) leads to

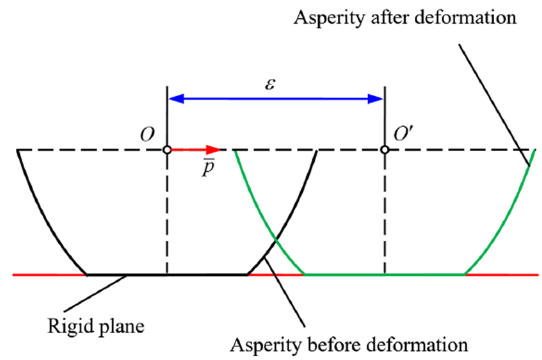

Fig. 7 Tangential contact of a single asperity

$$K_n = \frac{2E'\psi^{1-0.5D}Da_1^{0.5D}}{\sqrt{\pi}(1-D)}\left(a_1^{0.5-0.5D} - a_c^{0.5-0.5D}\right) \tag{19}$$

As shown in Fig. 7, the shear deformation ε produced by the tangential load $\overline{p}$ on a single asperity is described as [37]

$$\varepsilon = \frac{3(2-\nu)\mu p}{16G'r}\left(1 - \left(1 - \frac{\overline{p}}{\mu p}\right)^{\frac{2}{3}}\right), \quad G' = \frac{E'}{2(1+\nu)} \tag{20}$$

where G' represents the equivalent shear modulus of two contacting rough surfaces. μ denotes the coefficient of sliding friction. Then, the tangential compliance c_t of a single asperity is determined as

$$c_t = \frac{\mathrm{d}\varepsilon}{\mathrm{d}\overline{p}} = \frac{2-\nu}{8G'r}\left(1 - \frac{\overline{p}}{\mu p}\right)^{-\frac{1}{3}} \tag{21}$$

Assuming that the tangential and normal loads on the asperities are proportional to their contact area, the tangential contact stiffness of a single asperity is derived as

$$k_t = \frac{8G'r}{2-\nu}\left(1 - \frac{\overline{p}}{\mu p}\right)^{\frac{1}{3}} = \frac{8G'\sqrt{a}}{(2-\nu)\sqrt{\pi}}\left(1 - \frac{\overline{P}}{\mu P}\right)^{\frac{1}{3}} \tag{22}$$

where $\overline{P}$ denotes the resultant tangential force within a single-bolted joint's contact area. Obviously, the single asperity slides tangentially relative to the rigid plane when $\overline{P} > \mu P$. Integrating k_t within the contact area leads to the tangential contact stiffness of a single-bolted joint:

$$K_t = \int_{a_c}^{a_1} k_t n(a)\mathrm{d}a \tag{23}$$

Substituting Eqs. (11) and (22) into Eq. (23) leads to

$$K_t = \frac{8\psi^{1-0.5D}G'Da_1^{0.5D}}{(1-D)(2-\nu)\sqrt{\pi}}\left(1 - \frac{\overline{P}}{\mu P}\right)^{\frac{1}{3}}\left(a_1^{0.5-0.5D} - a_c^{0.5-0.5D}\right) \tag{24}$$

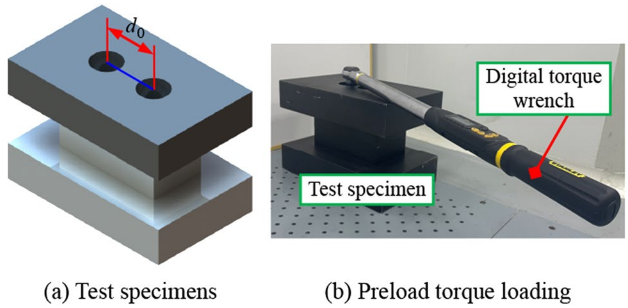

Fig. 8 Schematic of test specimens and preload torque loading equipment

According to Eqs. (19) and (24), the equivalent normal and tangential stiffnesses of a single-bolted joint are related to the elastic modulus, the tangential modulus, the fractal parameters, and the preload of the contact rough surfaces.

3 Experimental Verifications

In this section, we conducted modal analysis tests on two designed specimens and a box-in-box precision horizontal machine tool to demonstrate the accuracy and efficiency of the proposed contact stiffness model.

To illustrate the coupling effect, two test specimens made of HT300 were designed and assembled with different center distances between two adjacent bolted joints (70 mm and 100 mm), as shown in Fig. 8a. The bolts connecting the upper and lower surfaces in the two test specimens were identically M24 × 110, and the contact surfaces were machined using an accurate milling process. Assume that the machined surfaces have the same fractal dimension and roughness. The bolts in both test specimens were applied to identical preload torques of 340 Nm using a digital torque wrench (Stanley SD-340-22), as shown in Fig. 8b. Table 1 provides the material properties of the two contact surfaces, and Table 2 shows the mechanical parameters of a single-bolted joint.

Table 1 Material properties of HT300 gray cast iron

	E' (GPa)	$\overline{G}$(GPa)	ν	H (HV)	σ_y (MPa)	μ
Value	130	52	0.25	231	370	0.20

Table 2 Mechanical parameters of a single-bolted joint (preload: 340 Nm)

	r_0 (mm)	R_0 (mm)	α	B
Value	12	55	203.48	− 0.0305

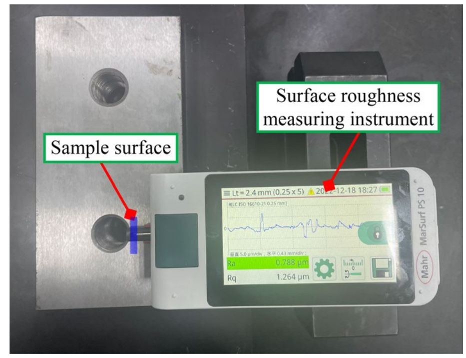

Fig. 9 Measurement of three-dimensional surface topography

3.1 Fractal Dimensions and Roughness Calculation

This subsection identifies machined rough surfaces' fractal dimension and roughness parameters.

Considering a 20 × 2.4-mm rectangular area in a rough surface as a sample surface, the topography height was measured by the surface roughness measuring instrument (MarSurf PS 10) illustrated in Fig. 9. The sensor precision of the instrument was 2 μm. The sample surface was composed of 21 measurement lines, and the probe moved along each measurement line for 2.4 mm. The measuring point interval Δx was 0.5 μm, leading to 4801 points for each measurement line. Figure 10 illustrates the three-dimensional topography of the milling surface.

Based on the structure function method, the function of the rough surface profile $S(\tau)$ is described as [38]

$$S(\tau) = \frac{1}{N-n}\sum_{i=0}^{N-n}\left(z(x_i+n)-z(x_i)\right)^2 \tag{25}$$

where $N-n$ represents the number of calculation data separated by an arbitrary interval $\tau = n \times \Delta x$ between the recorded data. The fractal dimension and roughness

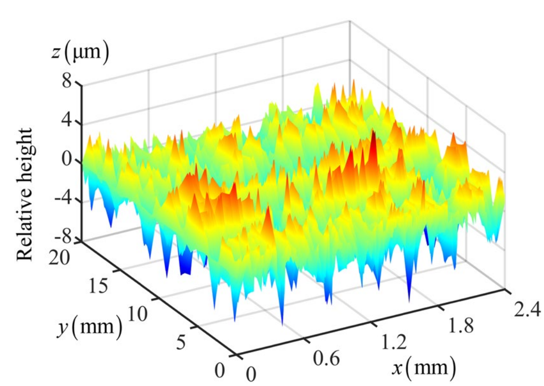

Fig. 10 Three-dimensional surface topography of the sample surface

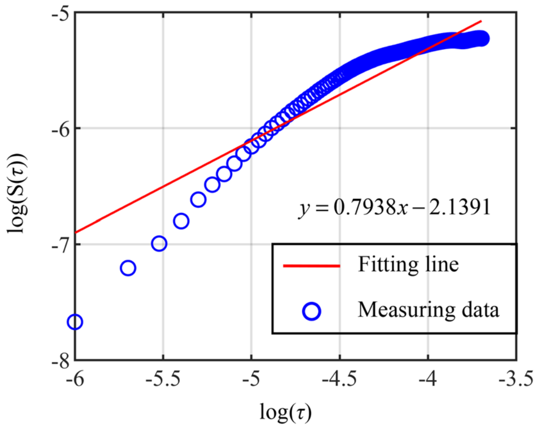

Fig. 11 Fitting line of the double logarithmic function of the measuring data in the middle line

parameters are then identified from double logarithmic coordinates as

$$
\begin{aligned}
&D = \frac{4-k}{2}, \quad \log G = \frac{b - \log C}{2(D-1)} \\
&C = \frac{\Gamma(2D-3)\sin(\pi(2D-3)/2)}{(4-2D)\ln\gamma}
\end{aligned}
\tag{26}
$$

where k and b represent the slope and intercept on the y-axis of the fitting line between $\log(S(\tau))$ and $\log(\tau)$. Figure 11 illustrates the fit line of the middle line (11th) in the sample surface when $n=25$, $k=0.7938$, and $b=-2.1391$. Thus, $D=1.6031$ and $G=1.90\times10^{-9}$ m. The fractal dimension and roughness parameters of the machined rough surfaces are calculated as the average value of 21 measurement lines, as shown in Table 3. Based on the proposed contact stiffness model, Table 4 provides the equivalent normal and tangential stiffnesses of a single-bolted joint in test specimens 1 and 2 without considering the coupling effect.

Table 3 Average fractal parameters of the machined surface of a test specimen

	R_a (μm)	D	G (m)
Value	0.786	1.598	1.972×10^{-9}

Table 4 Equivalent normal and tangential stiffnesses of a single-bolted joint under different conditions ($\times10^{10}$ N/m)

	K_{n1}	K_{t1}	K_{n2}	K_{t2}	$\hat{K}_n$	$\hat{K}_t$
Value	3.67	3.49	3.12	2.84	3.06	2.81

$K_{n1}(K_{t1})$ and $K_{n2}(K_{t2})$ represent the normal (tangential) contact stiffnesses of a single-bolted joint in test specimens 1 and 2. $\hat{K}_n\left(\hat{K}_t\right)$ is the normal (tangential) contact stiffness of a single-bolted joint without considering the coupling effect

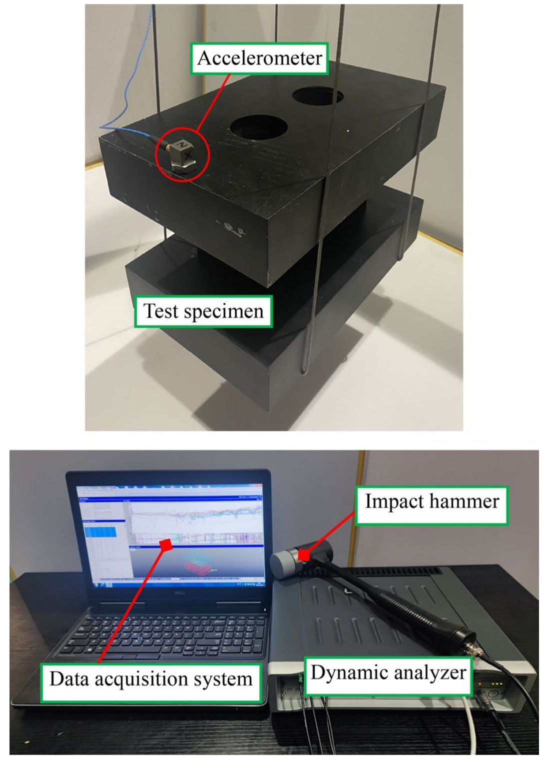

Fig. 12 Experimental setup for the modal test of the specimen 1

3.2 Modal Analysis Tests of the Test Specimens

This subsection conducts a modal test of the designed specimens to illustrate the accuracy of the proposed contact stiffness model.

Figure 12 illustrates the experimental setup for modal analysis tests on the designed specimens. During the experiment, the test specimens were suspended by steel wires to measure the free vibration modes. An impact hammer (ICP 086D20) was used to generate a transient excitation force on the test specimens, and an acceleration sensor (PCB 356A26) was employed to record vibration response signals from each measuring point. Then, using a dynamic testing and analysis system (SCADAS III), the data acquisition and post-processing of the excitation and response signals, as well as the identification of modal parameters, were accomplished, resulting in a detailed analysis of the results of the mode shapes of the test specimens.

Using the stiffness data in Table 4, the FEA models of the test specimens were established in SAMCEF commercial software. Each single-bolted joint was connected using a bushing unit, which was considered a virtual spring connecting the upper and lower specimens. The mesh type and average length of the upper and lower specimens were set as tetrahedral and 40 mm, respectively. The FEA software's corresponding boundary conditions and material

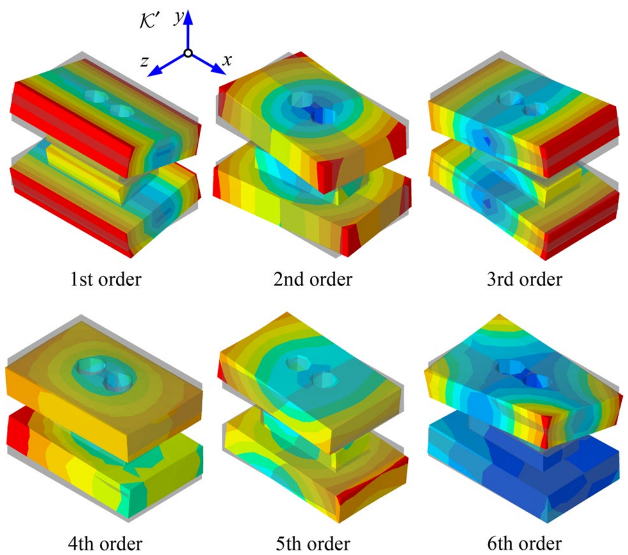

Fig. 13 First six mode shapes of test specimen 1 predicted by the FEA

properties were set consistent with those parameters of the test specimens, leading to an FEA model with 3.15×10^3 degrees of freedom. Figures 13 and 14 show the first six mode shapes of test specimen 1 ($d_0 = 70$ mm) obtained by the FEA and modal analysis tests, respectively. The first- and third-order mode shapes are the bending vibrations of the entire test specimen along the x- and z-directions of $\mathcal{K}'$, respectively. The second-order mode shape is a torsional vibration of the entire test specimen along the y-direction. The fourth-order mode shape is a translational vibration

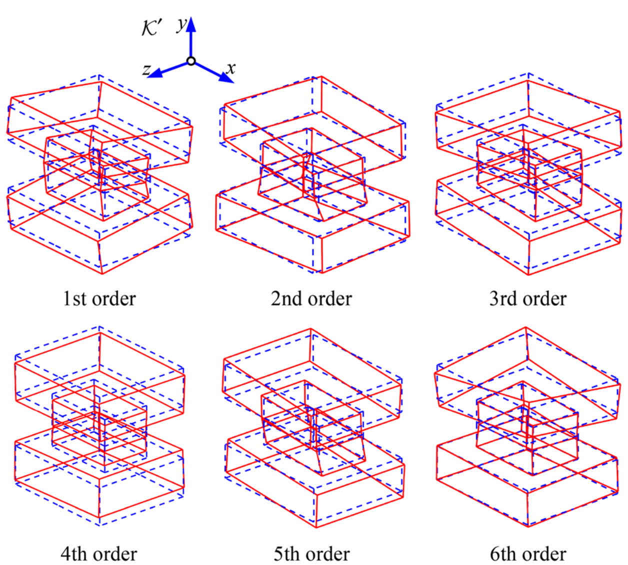

Fig. 14 First six mode shapes of test specimen 1 obtained from the modal test

of the upper and lower specimens along the y-direction, and the sixth-order mode shape is a local torsional vibration of the upper specimen. Obviously, the first six mode shape orders estimated by the FEA model agree very well with those obtained from modal tests. In addition, the MAC (modal assurance criterion) is employed to verify the above two models' consistency as

$$\mathrm{MAC}_{ij} = \frac{\left(\boldsymbol{\Phi}_{\mathrm{FE},i}^{\mathrm{T}} \boldsymbol{\Phi}_{\mathrm{MT},j}\right)^2}{\left(\boldsymbol{\Phi}_{\mathrm{FE},i}^{\mathrm{T}} \boldsymbol{\Phi}_{\mathrm{FE},i}\right)\left(\boldsymbol{\Phi}_{\mathrm{MT},j}^{\mathrm{T}} \boldsymbol{\Phi}_{\mathrm{MT},j}\right)}, \quad i,j = 1,2,\ldots,6 \tag{27}$$

where $\boldsymbol{\Phi}_{\mathrm{FE},i}$ and $\boldsymbol{\Phi}_{\mathrm{MT},j}$ are the ith and jth order mode shapes from the FEA and the developed modal test, respectively. Figure 15 shows the MAC of the first six mode shape orders of the two models. The diagonal elements' values are much higher than the remaining nondiagonal elements' values (0.95 against 0.23), demonstrating the accuracy of the developed contact stiffness model for calculating the mode shapes of the test specimen. In addition, the mode shapes of test specimen 2 ($d_0 = 100$ mm) obtained by the FEA and modal analysis tests are similar to those of specimen 1.

Tables 5 and 6 compare the errors in the natural frequencies of the first six orders of test specimens 1 and 2, respectively, for the FEA models and the modal test. The contact stiffnesses of bolted joints in FEA model 1 were calculated using the proposed model considering the coupling effect, which was ignored in FEA model 2. For test specimen 1, the natural frequencies predicted by model 1 are more accurate than those of model 2 (maximum error: 2.73% against −7.72%), illustrating the considerable impact of the coupling effect on a single-bolted joint's contact stiffness when d_0 is much smaller than $2R_0$. In contrast, for test specimen 2, the coupling effect can be negligible when d_0 is near $2R_0$. The above results illustrate the accuracy and efficiency of the proposed semi-analytical model for calculating the natural frequencies of the test specimen.

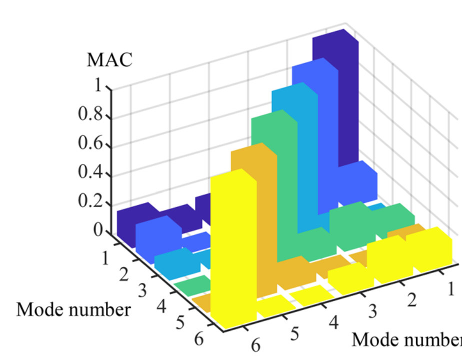

Fig. 15 MAC of the first six mode shape orders of test specimen 1 from the FEA and modal tests

Table 5 Natural frequencies of the first six mode orders of test specimen 1 obtained from an FEA and the modal test

	1st	2nd	3rd	4th	5th	6th
FEA model 1 (Hz)	817.09	1057.10	1620.96	2837.16	3498.04	3819.47
FEA model 2 (Hz)	751.77	967.42	1480.78	2564.89	3285.34	3562.71
Experimental results (Hz)	807.16	1048.32	1581.46	2761.85	3458.47	3778.29
Error 1 (%)	1.23	0.84	2.50	2.73	1.14	1.09
Error 2 (%)	−6.86	−7.72	−6.37	−7.13	−5.01	−5.71

The natural frequencies of FEA models 1 and 2 are obtained using $K_{n1}(K_{t1})$ and $\hat{K}_n(\hat{K}_t)$ in Table 4, respectively

Table 6 Natural frequencies of the first six mode orders of test specimen 2 obtained from an FEA and the modal test

	1st	2nd	3rd	4th	5th	6th
FEA model 1 (Hz)	822.01	1309.85	2115.33	3013.14	3566.68	3745.58
FEA model 2 (Hz)	821.63	1304.37	2112.29	3004.32	3561.84	3734.53
Experimental results (Hz)	814.68	1289.74	2080.19	2960.06	3529.34	3706.2
Error 1 (%)	0.90	1.56	1.69	1.79	1.06	1.06
Error 2 (%)	0.85	1.13	1.54	1.50	0.92	0.76

The natural frequencies of FEA models 1 and 2 are obtained using $K_{n2}(K_{t2})$ and $\hat{K}_n(\hat{K}_t)$ in Table 4, respectively

3.3 Modal Analysis Tests of the Entire Machine Tool

This subsection conducts a modal test of a box-in-box precision horizontal machine tool to illustrate the application of the proposed semi-analytical model in the dynamic predictions of an entire machine tool.

To increase the contact stiffness of a single-bolted joint while reducing the zero-pressure contact area in the fixed joint, the center distance d_0 between two adjacent bolts ($M24 \times 160$) was set to 80 mm. The preload torque of each bolt was set to 340 Nm. Based on the developed model considering the coupling effect, the normal and tangential contact stiffnesses of a single-bolted joint are 3.59×10^{10} N/m and 3.43×10^{10} N/m, respectively. Employing the dynamic model presented in [39], the dynamic responses of the tool and workpiece of the entire machine tool can be predicted. Meanwhile, a modal analysis test was performed on a prototype, as shown in Fig. 16. Figure 17 compares FRFs along the x-, y-, and z-axes of $\mathcal{K}'$ of the modal test and the employed dynamic model. Obviously, the FRFs of the employed model agree well with those of the modal test. Table 7 provides the natural frequencies of the experiments and the proposed model at the reference configuration. The differences between these two methods were less than 15.61%, demonstrating the accuracy and efficiency of the developed contact stiffness model of bolted joints and the employed dynamic model.

4 Conclusions

This article presents a semi-analytical approach for the normal and tangential contact stiffness modeling of bolted joints considering the coupling effect. The following inferences were drawn from the results obtained using the proposed method.

1. According to FEA simulation results, a nonlinear distribution model of contact stress inside a single-bolted joint is proposed using a negative exponential function. Subsequently, the analytical normal resultant force of the contact area of a single-bolted joint considering the coupling effect is derived based on the Hertz contact theory and FT, solving the largest microcontact area. Finally, the semi-analytical expressions for the normal and tangential contact stiffnesses of a single-bolted joint are formulated by integrating the stiffnesses of multi-asperities. The developed model indicates the influence of preload torque, material properties, center distance, and fractal parameters on the contact stiffnesses of bolted joints.
2. Considering two designed test specimens as illustrations, the effectiveness and accuracy of the presented model are demonstrated. The mode shapes of the two test specimens from a modal analysis test and the proposed model are highly consistent. The proposed model considering the coupling effect is more accurate than the traditional

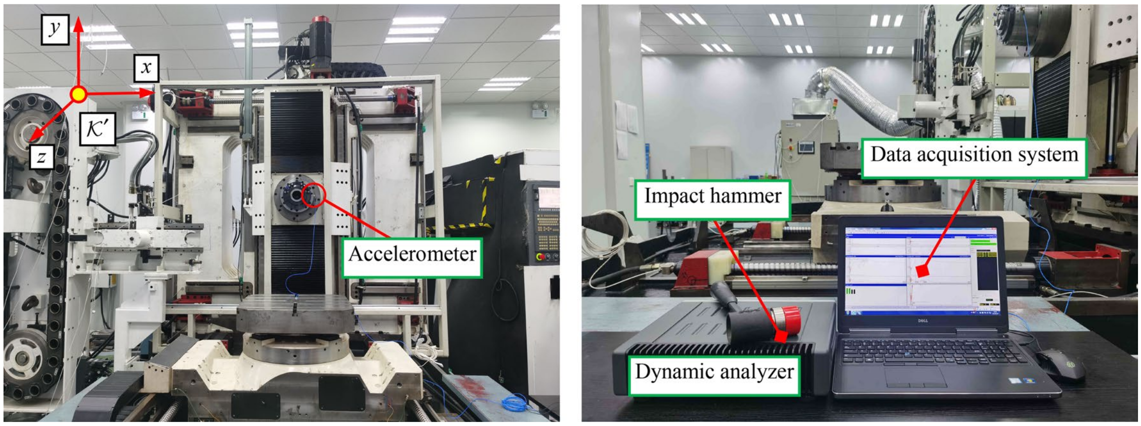

Fig. 16 Experimental setup for the modal test of a box-in-box precision horizontal machine tool

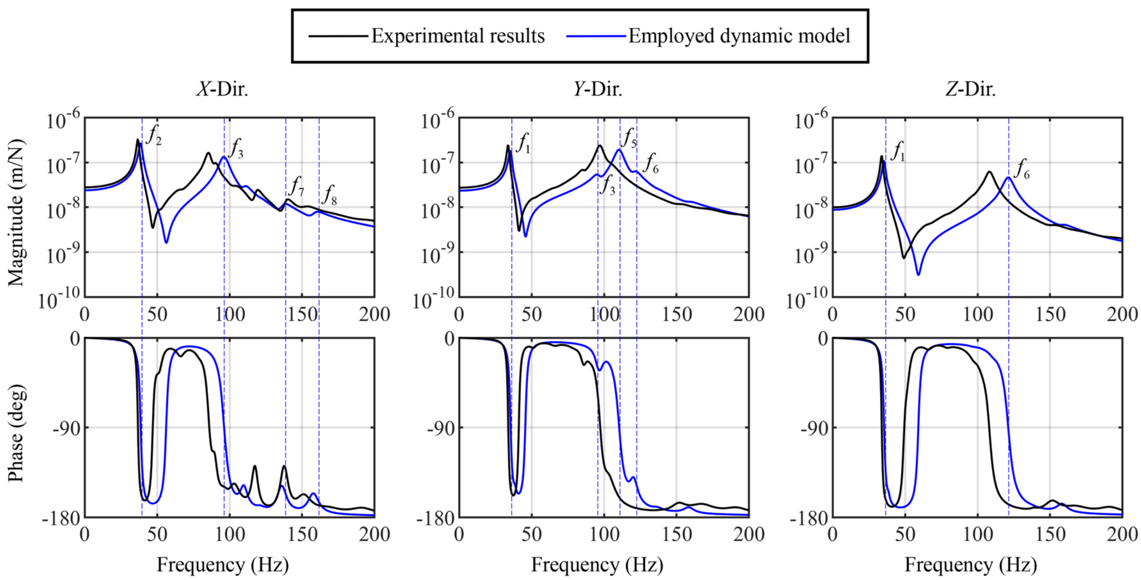

Fig. 17 FRF comparisons between the modal analysis test and the employed dynamic model

Table 7 Experimental and employed dynamic model natural frequencies of the entire machine tool at the reference configuration

Mode number	1st	2nd	3rd	4th	5th	6th	7th	8th
Employed dynamic model (Hz)	35.42	38.59	95.76	97.49	110.37	121.19	136.90	158.59
Experimental results (Hz)	33.82	36.71	85.60	90.29	97.21	108.19	118.42	138.93
Error (%)	4.73	5.12	11.87	7.97	13.54	12.02	15.61	14.15

method in predicting the contact stiffnesses of bolted joints. The maximum error in the natural frequencies of the proposed approach relative to experimental results is < 2.73%, illustrating the accuracy and efficiency of the developed contact stiffness model. In addition, a modal test on a box-in-box precision horizontal machine tool prototype illustrates the application of the proposed model in dynamic predictions of an entire machine tool. The developed approach is instrumental in revealing the influence of microcontact factors on the contact stiffness of bolted joints and in guiding the optimization of bolt arrangements.

Acknowledgements This work is partially funded by the EU Grant H2020-RISE-ECSASDPE (734272) and the China Scholarship Council (201908060118). Thanks are due to Tianjin University for assistance with the experiments.

Author Contributions All authors read and approved the final manuscript.

Data Availability The data supporting the findings of this study are available from the corresponding author upon reasonable request.

Declarations

Competing interests Xianping Liu is an editorial board member for "Nanomanfucturing and Metrology" and was not involved in the editorial review, or the decision to publish this article. All authors have no conflicts of interest that might have affected the publication of this study.

References

1. Weiser T, Corves B (2019) Deflection modeling of a manipulator for mechanical design. Mech Mach Theory 137:172–187. https://doi.org/10.1016/j.mechmachtheory.2019.03.025
2. Cao Y, Cao Z, Zhao Y et al (2020) Damage progression and failure of single-lap thin-ply laminated composite bolted joints under quasi-static loading. Int J Mech Sci 170:105360. https://doi.org/10.1016/j.ijmecsci.2019.105360
3. Deng C, Yin G, Fang H, Meng Z (2015) Dynamic characteristics optimization for a whole vertical machining center based on the configuration of joint stiffness. Int J Adv Manuf Technol 76:1225–1242. https://doi.org/10.1007/s00170-014-6355-9
4. Chang Y, Ding J, He Z et al (2020) Effect of joint interfacial contact stiffness on structural dynamics of ultra-precision machine tool. Int J Mach Tools Manuf 158:103609. https://doi.org/10.1016/j.ijmachtools.2020.103609
5. Liu YP, Altintas Y (2022) Predicting the position-dependent dynamics of machine tools using progressive network. Precis Eng 73:409–422. https://doi.org/10.1016/j.precisioneng.2021.10.010
6. Mao K, Li B, Wu J, Shao X (2010) Stiffness influential factors-based dynamic modeling and its parameter identification method of fixed joints in machine tools. Int J Mach Tools Manuf 50:156–164. https://doi.org/10.1016/j.ijmachtools.2009.10.017
7. Xu C, Zhang J, Wu Z et al (2013) Dynamic modeling and parameters identification of a spindle-holder taper joint. Int J Adv Manuf Technol 67:1517–1525. https://doi.org/10.1007/s00170-012-4586-1
8. Xiao W, Mao K, Li B, Lei S (2014) Contact stiffness of bolted joint with different material combination in machine tools. J Vibroeng 16(7):3281–3293
9. Abad J, Medel FJ, Franco JM (2014) Determination of Valanis model parameters in a bolted lap joint: experimental and numerical analyses of frictional dissipation. Int J Mech Sci 89:289–298. https://doi.org/10.1016/j.ijmecsci.2014.09.014
10. Mehrpouya M, Sanati M, Park SS (2016) Identification of joint dynamics in 3D structures through the inverse receptance coupling method. Int J Mech Sci 105:135–145. https://doi.org/10.1016/j.ijmecsci.2015.11.007
11. Li D, Xu C, Liu T et al (2019) A modified IWAN model for micro-slip in the context of dampers for turbine blade dynamics. Mech Syst Signal Process 121:14–30. https://doi.org/10.1016/j.ymssp.2018.11.002
12. Li C, Zhang Z, Yang Q, Li P (2020) Experiments on the geometrically nonlinear vibration of a thin-walled cylindrical shell with points supported boundary condition. J Sound Vib 473:115226. https://doi.org/10.1016/j.jsv.2020.115226
13. Li C, Jiang Y, Qiao R, Miao X (2021) Modeling and parameters identification of the connection interface of bolted joints based on an improved micro-slip model. Mech Syst Signal Process 153:107514. https://doi.org/10.1016/j.ymssp.2020.107514
14. Majumdar A, Tien CL (1990) Fractal characterization and simulation of rough surfaces. Wear 136(2):313–327. https://doi.org/10.1016/0043-1648(90)90154-3
15. Majumdar A, Bhushan B (1991) Role of fractal geometry in roughness characterization and contact mechanics of surfaces. J Tribol 112(2):205–216. https://doi.org/10.1115/1.2920243
16. Liu P, Zhao H, Huang K, Chen Q (2015) Research on normal contact stiffness of rough surface considering friction based on fractal theory. Appl Surf Sci 349:43–48. https://doi.org/10.1016/j.apsusc.2015.04.174
17. Chen Q, Xu F, Liu P, Fan H (2016) Research on fractal model of normal contact stiffness between two spheroidal joint surfaces considering friction factor. Tribol Int 97:253–264. https://doi.org/10.1016/j.triboint.2016.01.023
18. Pan W, Li X, Wang L et al (2017) A normal contact stiffness fractal prediction model of dry-friction rough surface and experimental verification. Eur J Mech A/Solids 66:94–102. https://doi.org/10.1016/j.euromechsol.2017.06.010
19. Wang R, Zhu L, Zhu C (2017) Research on fractal model of normal contact stiffness for mechanical joint considering asperity interaction. Int J Mech Sci 134:357–369. https://doi.org/10.1016/j.ijmecsci.2017.10.019
20. Xiao H, Sun Y, Chen Z (2019) Fractal modeling of normal contact stiffness for rough surface contact considering the elastic–plastic deformation. J Braz Soc Mech Sci Eng 41:1–13. https://doi.org/10.1007/s40430-018-1513-x
21. Pan W, Li X, Wang L et al (2018) Influence of contact stiffness of joint surfaces on oscillation system based on the fractal theory. Arch Appl Mech 88:525–541. https://doi.org/10.1007/s00419-017-1325-y
22. Guan D, Jing L, Gong J et al (2018) Normal contact analysis for spherical pump based on fractal theory. Tribol Int 124:117–123. https://doi.org/10.1016/j.triboint.2018.04.002
23. Liu J, Ma C, Wang S et al (2019) Contact stiffness of spindle-tool holder based on fractal theory and multi-scale contact mechanics model. Mech Syst Signal Process 119:363–379. https://doi.org/10.1016/j.ymssp.2018.09.037
24. Zhang K, Li G, Gong JZ, Zhang M (2019) Normal contact stiffness of rough surfaces considering oblique asperity contact. Adv Mech Eng 11(1):1–14. https://doi.org/10.1177/1687814018824471
25. Liu Z, Jiang K, Zhang C et al (2020) A stiffness model of a joint surface with inclination based on fractal theory. Precis Eng 62:47–61. https://doi.org/10.1016/j.precisioneng.2019.10.012
26. Chang Y, Ding J, Fan H et al (2022) A hybrid method for bolted joint modeling considering multi-scale contact mechanics. Precis Eng 78:171–188. https://doi.org/10.1016/j.precisioneng.2022.08.001
27. Tian H, Li B, Liu H et al (2011) A new method of virtual material hypothesis-based dynamic modeling on fixed joint interface in machine tools. Int J Mach Tools Manuf 51:239–249. https://doi.org/10.1016/j.ijmachtools.2010.11.004

28. Guo H, Zhang J, Feng P et al (2015) A virtual material-based static modeling and parameter identification method for a BT40 spindle–holder taper joint. Int J Adv Manuf Technol 81:307–314. https://doi.org/10.1007/s00170-014-6376-4
29. Liao J, Zhang J, Feng P et al (2016) Interface contact pressure-based virtual gradient material model for the dynamic analysis of the bolted joint in machine tools. J Mech Sci Technol 30:4511–4521. https://doi.org/10.1007/s12206-016-0919-6
30. Ye H, Huang Y, Li P et al (2016) Virtual material parameter acquisition based on the basic characteristics of the bolt joint interfaces. Tribol Int 95:109–117. https://doi.org/10.1016/j.triboint.2015.11.013
31. Zhao Y, Yang C, Cai L et al (2016) Surface contact stress-based nonlinear virtual material method for dynamic analysis of bolted joint of machine tool. Precis Eng 43:230–240. https://doi.org/10.1016/j.precisioneng.2015.08.002
32. Xiao H, Sun Y (2018) An improved virtual material based acoustic model for contact stiffness measurement of rough interface using ultrasound technique. Int J Solids Struct 155:240–247. https://doi.org/10.1016/j.ijsolstr.2018.07.026
33. Zhang K, Li G, Gong J, Wan F (2019) Modal analysis of bolted structure based on equivalent material of joint interface. Materials 12(18):3004. https://doi.org/10.3390/ma12183004
34. Yang Y, Cheng H, Liang B et al (2021) A novel virtual material layer model for predicting natural frequencies of composite bolted joints. Chin J Aeronaut 34:101–111. https://doi.org/10.1016/j.cja.2020.05.028
35. Majumdar A, Bhushan B (1991) Fractal model of elastic–plastic contact between rough surfaces. J Tribol 113(1):1–11. https://doi.org/10.1115/1.2920588
36. Wang S, Komvopoulos K (1994) A fractal theory of the interfacial temperature distribution in the slow sliding regime: part I—elastic contact and heat transfer analysis. J Tribol 116(4):812–822. https://doi.org/10.1115/1.2927338
37. Mindlin RD, Deresiewicz H (1953) Elastic spheres in contact under varying oblique forces. J Appl Mech 20(3):327–344
38. Xu M, Li C, Yao G et al (2022) Load-dependent stiffness model and experimental validation of four-station rotary tool holder. Mech Syst Signal Process 171:108868. https://doi.org/10.1016/j.ymssp.2022.108868
39. Ma Y, Tian Y, Liu X (2023) Rapid predictions for lower-order dynamics of machine tools based on the rigid multipoint constraints. Int J Precis Eng Manuf 24:485–500. https://doi.org/10.1007/s12541-022-00761-9

Yiwei Ma received the bachelor's degree from Tianjin University, Tianjin, China, in 2017. He is currently working toward the Ph.D. degree in mechanical engineering with the School of Engineering, University of Warwick, Coventry, U.K. His research interests include stiffness and dynamic modeling of machine tools, dynamic optimization design, and hybrid or parallel machine tools.

Yiwei Fu received the bachelor's degree from Tianjin University, Tianjin, China, in 2017. He is currently working toward the Ph.D. degree in mechanical engineering with the School of Mechanical Engineering, Tianjin University, Tianjin, China. His research interests include stiffness and dynamic modeling and simulations of machine tools.

Yanling Tian received the Ph.D. degree in mechatronics engineering from Tianjin University, Tianjin, China, in 2005. He is an Associate Professor with the School of Engineering, University of Warwick, Coventry, U.K. Prior to joining Warwick University, he held the Research Fellowship with Monash University, Melbourne, Australia, Alexander von Humboldt Fellowship for Experienced Researchers with Oldenburg University, Oldenburg, Germany, and Marie Curie Fellowship with Warwick University. He is the Fellow of Higher Education Academy (FHEA), Heslington, U.K. He has authored or coauthored more than 200 high-ranking journals and peer-reviewed conference papers. His research interests include micro/nano robotics and automation, precision instrument design and modeling and control, metrology and characterization, and mechanobiology and biomechanics. Dr. Tian was a Technical Editor for IEEE-ASME TRANSACTIONS ON MECHATRONICS from 2015 to 2020.

Xianping Liu received the Ph.D. degree in Centre for Nanotechnology and Microengineering, Department of Engineering, University of Warwick, Coventry, U.K. She is currently a professor with the School of Engineering, University of Warwick, Coventry, U.K. She is the expert panel member for European REA-FP7-NMP, and the fellow of Institute of Nanotechnology and Royal Microscopical Society. She has authored or coauthored more than 100 high-ranking journals and peer-reviewed conference papers. Her research interests include Precision Engineering, Surface Measurement and Chracterisation, Micro/Nanotribology, Nanometrology, Sensors and actuators, and Development of a Novel Tribological Probe Microscope (TPM) for measuring surface's geometrical, mechanical and tribological properties.